Influence of induced magnetic fields on Shapiro steps in Josephson-junction arrays

J. R. Phillips, H. S. J. van der Zant, J. White, and T. P. Orlando
Department of Electrical Engineering and Computer Science, Massachusetts Institute of Technology, Cambridge, Massachusetts 02139
(Received 13 October 1993; revised manuscript received 13 May 1994)

Using numerical simulation, we study the effect of self-induced magnetic fields on the properties of Josephson-junction arrays driven with combined ac and dc currents. We show that inductive effects in strongly overdamped arrays can induce subharmonic giant Shapiro steps in zero applied magnetic field. Inductive effects can also reduce the range of dc current biases over which the array can lock to the ac current. Calculation of the correct current-voltage characteristics of the array requires considering mutual inductance interactions between all cells in the array. We also discuss efficient numerical schemes for including these induced fields in dynamic simulation of Josephson arrays.

I. INTRODUCTION

There has been much recent interest in the properties of Josephson-junction arrays driven by dc and ac currents, particularly in the study of fractional giant[1] and subharmonic[2,3] Shapiro step structure. While the occurrence of fractional steps in a magnetic field seems to be explained by a phenomenological model of a moving vortex superlattice,[4–7] the origin of subharmonic structure, particularly in zero applied field, is less clear. Several explanations have been proposed,[8–10] including inductive (self-field) effects.[2,11] There has also been long-standing interest in the use of Josephson arrays as coherent microwave sources, and recently an observation of coherent emission from two-dimensional (2D) Josephson-junction arrays was reported.[12] The arrays used in the experiments of Ref. 12 had high critical currents, indicating that the strength of the magnetic fields induced in these arrays by circulating supercurrents is fairly large. However, there have been relatively few studies of Josephson arrays that consider the effect of induced magnetic fields, and most of the previous treatments have severely approximated the form of the induced fields.

In this paper, we discuss dynamic simulation of 2D Josephson arrays, where inductive effects are important. We have included the mutual inductance interactions between all cell pairs in the arrays, as they are necessary to calculate the correct screening properties of the induced fields.[13] In Sec. II we discuss our numerical technique for dynamic simulation of Josephson junction arrays when self-field effects are included. In Sec. III we give a qualitative description of some of the effects that induced fields have on Shapiro-step structure in overdamped arrays, particularly in zero applied magnetic field. We find that induced magnetic fields can produce subharmonic Shapiro step structure in zero applied magnetic field, and we give a qualitative description of the movement of vortices on the subharmonic Shapiro steps. Although the symmetry-breaking effect of the self-fields can generate subharmonic Shapiro steps, the steps do not appear to be due to the formation of an induced commensurate vortex state at the edges of the array, as was proposed in Ref. 2. Another effect of the self-fields is that in arrays with penetration depths small relative to the size of the array, such as in Refs. 8, 12, and 14, the screening effects due to induced fields may be strong enough to destroy phase locking over some parameter range, significantly reducing the width of the giant Shapiro steps.

It has been previously demonstrated see (Ref. 11) that inductive effects can generate subharmonic Shapiro steps. We are in agreement with Ref. 11 in that we find subharmonic structure can arise as a result of induced fields. Our work differs from Ref. 11 in that we have considered inductive interactions between all array cell pairs (full inductance matrix), whereas the model of Ref. 11 only considers inductive interations between cells very close together (truncated mutual-inductance matrix), and thus may produce current-voltage (I-V) characteristics which are different from ours. Such approximate models are fairly widely used (e.g., Refs. 15 and 16), so it is thus of interest to consider the properties of approximate inductance models in the presence of applied currents. In the Shapiro-step context, we find that the stronger screening implied by the truncation of the inductance matrix may anomalously destroy phase locking.

II. NUMERICAL PROCEDURE

The general aspects of including self-field effects in simulation of Josephson arrays have previously been discussed in Ref. 13. Here we extend the approach to include junction dynamics and applied currents. To model the dynamics of the junction we include contributions to the junction current from resistive and capacitive shunts. Including applied currents in mesh-based analysis of the Josephson array is also fairly straighforward; it is simply necessary to include additional meshes corresponding to current sources. We also describe improvements to the iterative technique presented in Ref. 13 which further accelerate the dynamic simulation of Josephson arrays.

0163-1829/94/50(13)/9387(10)/$06.00

A. Formulation

The first set of variables describing the array are the gauge-invariant phase differences ϕ across each junction in the array. The directed sum of the phase differences around each cell is related to the flux Φ passing through the cell by[11,13,15,16]

$$M\phi = -2\pi\frac{\Phi}{\Phi_0} + 2\pi n \ , \tag{1}$$

where M is the mesh matrix,[17] which represents the directed loop-sum operator, n is a vector of integers, and Φ_0 is the flux quantum. The flux can be split into an induced part $\Phi^{\rm ind}$ and an applied part $\Phi^{\rm ext}$. In the absence of applied currents, the induced flux $\Phi^{\rm ind}_{i,j}$ in each cell i,j is calculated by summing the flux contributions from mesh (loop) currents $I^m_{i',j'}$ flowing in all cells i',j' of the array:

$$\Phi^{\rm ind}_{i,j} = \sum_{i',j'} L_{i,i',j,j'} I^m_{i',j'} \ , \tag{2}$$

where $L_{i,i',j,j'}$ is the mutual inductance coefficient between cells (i,j) and (i',j') and the sum is taken over all cells (i',j'). In vector notation,

$$\Phi^{\rm ind} = LI_m \ , \tag{3}$$

where I_m is the vector of mesh currents and L the inductance matrix.

To calculate the induced fields in the presence of applied currents, it is simplest to work first in terms of the branch (junction) currents I_J and branch inductance matrix L^b. As discussed in Ref. 13, the induced flux is

$$\Phi^{\rm ind} = ML^bI_J \ . \tag{4}$$

I_J can be expressed in terms of the mesh currents I_m and the externally applied currents. We define the vector I_s to be the contribution to each junction current from the applied sources, so that the junction currents can be written as

$$I_J = M^TI_m + I_s \ , \tag{5}$$

where the superscript T denotes matrix transpose. Therefore, the induced flux is given by

$$\Phi^{\rm ind} = LI_m + ML^bI_s, \tag{6}$$

where $L \equiv ML^bM^T$. Combining Eqs. (1) and (6) produces

$$M\phi + \frac{2\pi}{\Phi_0}[LI_m + ML^bI_s] = 2\pi(n-f) \ , \tag{7}$$

where we have made the usual definition of the frustration, $f = \Phi^{\rm ext}/\Phi_0$.

The current I_J through a junction with resistive and capacitive shunts is

$$I_J = I_c\sin\phi + \frac{v}{R_n} + C\frac{dv}{dt} \ , \tag{8}$$

where I_c is the junction critical current, v is the voltage across the junction, R_n is the normal-state resistance, and C is the junction capacitance. Equations (5) and (8) can be combined to express the junction currents I_J in terms of the mesh currents I_m:

$$M^TI_m + I_s = I_c\sin\phi + \frac{v}{R_n} + C\frac{dv}{dt}. \tag{9}$$

The final equation necessary to describe the dynamic Josephson array is the voltage-phase relation

$$v = \frac{\Phi_0}{2\pi}\frac{d\phi}{dt}. \tag{10}$$

It is convenient to normalize time to $\tau_c \equiv 1/\nu_c \equiv \Phi_0/I_cR_n$, current to I_c, and voltage to I_cR_n. In these units, Eqs. (7), (9), and (10) become

$$\frac{\beta_c}{2\pi}\frac{dv}{dt} = M^TI_m - \sin\phi - v + I_s \ , \tag{11a}$$

$$\frac{d\phi}{dt} = 2\pi v \ , \tag{11b}$$

$$M\phi + \frac{1}{\lambda_\perp}[\Lambda I_m + M\Lambda^bI_s] = 2\pi(n-f) \ , \tag{11c}$$

where $\beta_c = 2\pi I_cR_n^2C/\Phi_0$ is the McCumber parameter, $\lambda_\perp = \Phi_0/2\pi I_c\mu_0 p$ is the dimensionless penetration depth for a 2D system,[18] and $\Lambda = L/\mu_0 p$, $\Lambda^b = L^b/\mu_0 p$ with p the array lattice spacing, are the normalized inductance matrices.

The system of Eq. (11) can be viewed either as a nonlinear system of differential-algebraic equations (DAE's), or as implicitly defining a set of ordinary differential equations (ODE's). The system of ODE's can be explicitly written in normal form by eliminating the mesh currents as unknowns:

$$\frac{\beta_c}{2\pi}\frac{dv}{dt} = \lambda_\perp M^T\Lambda^{-1}[2\pi(n-f) - M\phi - ML^bI_s] - \sin\phi - v + I_s \ , \tag{12a}$$

$$\frac{d\phi}{dt} = 2\pi v \ . \tag{12b}$$

If the array is highly overdamped (very small β_c), the capacitive term of the junction current may be ignored, in which case Eqs. (12a) and (12b) can be combined as

$$\frac{1}{2\pi}\frac{d\phi}{dt} = \lambda_\perp M^T\Lambda^{-1}[2\pi(n-f) - M\phi - ML^bI_s] - \sin\phi + I_s. \tag{13}$$

B. Algorithms

The most obvious approach to solving Eq. (12) or Eq. (13) is to use some sort of explicit integration scheme (we use a predictor-corrector scheme based on the multistep Adams formulas.[19]) Regardless of the particular scheme used, the primary computational expense will be in solving linear systems of the form

$$\Lambda I_m = \lambda_\perp[2\pi(n-f) - M\phi - ML^bI_s] \ . \tag{14}$$

As the calculation of a complete I-V characteristic requires the simulation of the array over many ac cycles at many different dc current biases, thousands or millions of solutions of Eq. (14) may be required, so it is important to use an efficient scheme to solve Eq. (14). For small arrays, an efficient approach is to compute the LU factorization[20] of Λ and then perform a back substitution every time a right-hand-side evaluation is required. If there are N cells in the array, the initial factorization requires $O(N^3)$ operations and each back substitution requires $O(N^2)$ operations. $O(N^2)$ memory is needed to store the factored Λ. In larger arrays, the $O(N^2)$ time required for a back substitution may become considerable, the need for $O(N^2)$ storage may become cumbersome, and the $O(N^3)$ time required for the initial LU factorization may become unacceptably large. When this is the case, Eq. (14) can be solved by an FFT-accelerated iterative method,[13] which requires $O(N \log_2 N)$ time for each system solution.

The FFT-accelerated approach is easily derived by noting that if a conjugate-direction style iterative method [we use GMRES (Ref. 21)] is used to solve the linear system $\Lambda x = b$, the residual $r = b - \Lambda x$, must be computed at each iteration. If the number of iterations is much less than N, the primary computational cost of each iteration will be the computation of the matrix-vector product Λx. As Λ is dense, this will require $O(N^2)$ operations if done directly, but the special form of Λ implies Λx can be computed in $O(N \log_2 N)$ operations by using the FFT.[13]

The convergence of GMRES can be accelerated by applying the method to solving the preconditioned problem $\Lambda P y = b$ and then computing $x = Py$. If P is close to Λ^{-1} the convergence of GMRES will be rapid. One approach[13] is to define $\tilde{\Lambda}$ to be the part of Λ corresponding to self and nearest-neighbor inductances, and then set $P^{-1} = \tilde{\Lambda}$. A more effective preconditioner can be constructed by exploiting the fact that Λ is constant in Eq. (14) at each time step.

To derive this preconditioner, let S denote the discrete sine transform operator and let X_ϵ denote an operator that discards off-diagonal matrix elements less than or equal to ϵ times the smallest diagonal matrix element. Then an effective preconditioner is $P_\epsilon = S^T[X_\epsilon(S\Lambda^{-1}S^T)]S$ for some ϵ, as the matrix $S\Lambda^{-1}S^T$ is nearly diagonal.[13] Clearly $P_0 = \Lambda^{-1}$, which gives excellent convergence but is costly to apply at each iteration, and P_1 is almost $\tilde{\Lambda}^{-1}$. A choice of $\epsilon = 10^{-3}$ results in GMRES convergence in few (4–5) iterations and also yields a very sparse P_ϵ so each iteration is computationally inexpensive.

$S\Lambda^{-1}S^T$, and therefore P_ϵ, can also be computed in an efficient manner. Column i of $S\Lambda^{-1}S^T$ can be obtained by solving the system

$$S\Lambda S^T x_i = e_i \ , \tag{15}$$

where e_i is the ith unit vector and x_i is the ith column of $S\Lambda^{-1}S^T$. This system can be solved by an FFT-accelerated iterative method in roughly $O(N \log_2 N)$ time, so that the time to compute P_ϵ is roughly $O(N^2 \log_2 N)$. Since each column x_i can be calculated in turn and small elements discarded, the storage required for computation of $X_\epsilon(S\Lambda^{-1}S^T)$ is substantially less than the $O(N^2)$ memory necessary to store the full Λ^{-1}. For a 95×95 array, with $\epsilon = 10^{-3}$, about 2×10^4 elements are retained in $X_\epsilon(S\Lambda^{-1}S^T)$, a factor of 2×10^{-3} fewer than in the full factored Λ.

Finally, we note that it may be the case that the underlying system of ordinary differential equations [Eq. (12)] is stiff,[22] particularly for when the system is large, β_c is small, or $\lambda_\perp$ is large. In this case stiffly-stable implicit integration schemes are more efficient and robust, but require the solution of a nonlinear system of equations at each time step. The nonlinear systems are generally solved using Newton's method,[23] which results in a system of linear equations to be solved at each Newton iteration. Because these linear systems involve the dense matrix Λ, and are different at each Newton iteration (and therefore at each time step), solution by direct LU factorization is inefficient as the computation time will be $O(N^3)$ for every timestep. Again, an FFT-accelerated preconditioned iterative technique can be used to solve these system. The details of implementation are further discussed in the Appendix.

In all cases, the order and stepsize of the integration formulas are chosen automatically to maximize the step size, while restricting the estimated integration error per step to be less than a specified error tolerance. We have generally required the integration error per step to be less than 10^{-4} in the normalized units of Eq. (11). The details of implementation of our integration scheme are similar to Refs. 24 and 25.

III. RESULTS

We have computed the time-averaged current-voltage characteristics of Josephson-junction arrays subject to combined dc and ac currents for a variety of ac current amplitudes, frequencies, and screening lengths $\lambda_\perp$. A current $I = I_{\rm dc} + I_{\rm ac} \sin 2\pi\nu_I t$ was injected uniformly into each node along one edge of the array. The dc current $I_{\rm dc}$ was stepped in intervals of at most $0.01\ I_c$ (per node). We have generally taken zero initial conditions in all variables, which is the ground state for an array with no applied current, in zero field, at zero temperature. Several simulations were performed with random initial conditions and no change in the results was observed. At each dc bias point, the array was simulated for about 100 ac cycles to let transients settle, and then the time-average voltage $\overline{v}$ across the array was computed over an interval T. Generally $T \simeq 100/\nu_I$ (100 ac cycles), except that when a state with periodicity $T = 1/\nu_I$, $2/\nu_I$, or $3/\nu_I$ was found the voltage was extracted from one period of the array average voltage wave form. More precisely, the instantaneous average voltage across the array $V(t)$ is

$$V(t) = \frac{1}{N_I} \sum_{i:v_i \parallel I} v_i, \tag{16}$$

where the sum is taken over all junctions i parallel to

the direction of applied current, and N_I is the number of junction lines parallel to the current ($N_I = N + 1$ for an $N \times N$ cell array). The time-averaged voltage across the array is

$$\overline{v} = \frac{1}{T}\int_0^T V(t)\,dt = \frac{1}{N_I}\frac{1}{2\pi T}\sum_{i:\phi_i \parallel I}[\phi_i(T) - \phi_i(0)]\ . \tag{17}$$

A. Subharmonic Shapiro step structure

In Fig. 1 we show representative current-voltage characteristics of an overdamped ($\beta_c = 0$) 11×11 cell array in zero applied field, with the ac frequency $\nu_I = 0.6\nu_c$ and amplitude $I_{ac} = I_c$. The first integer giant Shapiro step is clearly visible at $\overline{v}/\nu_I N\Phi_0 = 1$ for all values of $\lambda_\perp$. At high $\lambda_\perp$, this is the only visible structure. At lower $\lambda_\perp$ ($\lambda_\perp$ less than the system size), $\frac{1}{2}$ and $\frac{3}{2}$ steps become visible. At still smaller $\lambda_\perp$, higher-order subharmonic steps become visible, in Fig. 1 (a) most prominently at $\frac{1}{4}$, $\frac{1}{3}$, $\frac{2}{3}$, $\frac{4}{5}$, $\frac{4}{3}$, and $\frac{3}{2}$. The other notable effect of the self-fields is the decrease of the width of the integer step at lower $\lambda_\perp$, a point to which we will return in the next section. Figure 2 shows I-V curves for a higher frequency ($\nu_I = 2\nu_c$) and driving current ($I_{ac} = 2.0I_c$). The I-V curves have a somewhat different shape, but the effects on Shapiro-step structure are qualitatively similar: self-field effects reduce the width of the integer giant Shapiro steps, and introduce subharmonic structure. Note that for these parameters, the $\frac{1}{2}$ step persists to larger $\lambda_\perp$ (at least $\lambda_\perp = 10$) than for the parameters of Fig. 1.

Spectral analysis of the array voltage $V(t)$ provides some insight into the Josephson array dynamics on a subharmonic step. In frequency analysis of the Josephson array, we use an estimator $\tilde{V}(\nu)$ of the spectral content of $V(t)$ calculated by a periodogram technique.[26] As shown in Fig. 3, spectral analysis of the voltage across the Josephson array reveals strong structure at the expected subharmonic frequencies. The solid curve of Fig. 3 shows the spectral content $\tilde{V}(\nu)$ of the average array voltage $V(t)$ when the 11×11 array of Fig. 1(a) is biased on the $\frac{1}{3}$ subharmonic step. As expected, there are peaks in $\tilde{V}(\nu)$ only at $\nu_I/3$ and its harmonics, indicating a process with periodicity $3/\nu_I$. We have also examined instances where a subharmonic step with finite slope is present, indicating that the array is not completely phase locked [e.g., part of the $\frac{1}{2}$ step in Figs. 1(b) and 2(c)], in which case the spectral function $\tilde{V}(\nu)$ still exhibits subharmonic structure, but with a background noise level several orders of magnitude higher. The dashed curve in Fig. 3 shows $\tilde{V}(\nu)$ computed when the array was biased on the $\frac{1}{2}$ step of Fig. 1(b) at a point where the array was not precisely locked to the applied current. This behavior indicates a weak tendency for the array to phase lock to the oscillating driving current, as we would expect to occur for the subharmonic steps as $\lambda_\perp$ is increased.

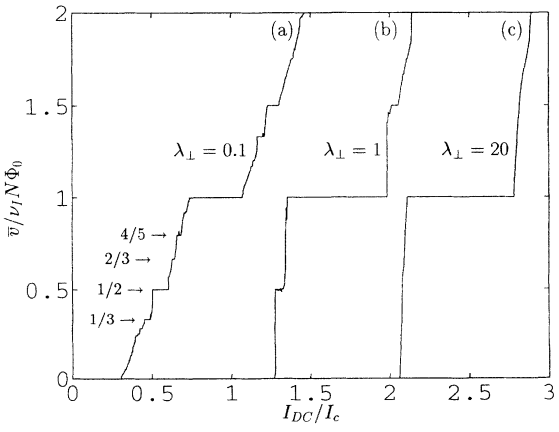

FIG. 1. Zero-field I-V characteristics of ac-driven 11×11 cell array, $\beta_c = 0.0$, $\nu_I = 0.6\nu_c$, $f = 0.0$, $I_{ac} = 1.0I_c$. The horizontal axis is I_{dc}, which is the dc current injected per node at the edge of array. The vertical axis is time-averaged voltage $\overline{v}$ normalized to $N\Phi_0\nu_I$. (a) $\lambda_\perp = 0.1$, (b) $\lambda_\perp = 1$, and (c) $\lambda_\perp = 20$. Successive curves are displaced along the horizontal axis by 0.75 units.

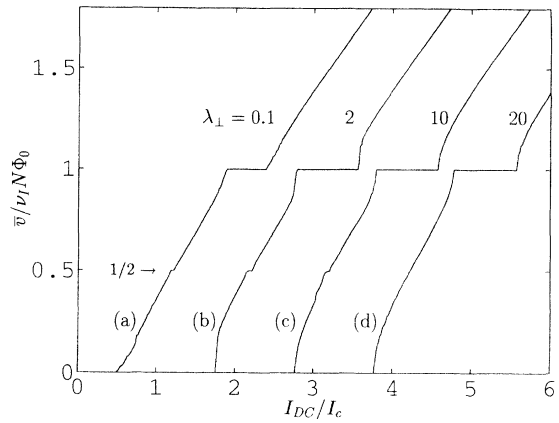

FIG. 2. Zero-field I-V characteristics of ac-driven 11×11 array, $\beta_c = 0.0$, $\nu_I = 2.0\nu_c$, $f = 0.0$, and $I_{ac} = 2.0I_c$. (a) $\lambda_\perp = 0.1$, (b) $\lambda_\perp = 2$, (c) $\lambda_\perp = 10$, and (d) $\lambda_\perp = 20$. Successive curves are displaced along the horizontal axis by 1.0 units.

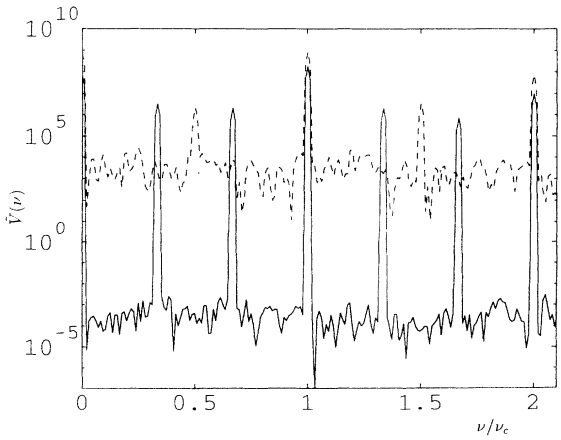

FIG. 3. Spectrum analysis $\tilde{V}(\nu)$ of the array average voltage $V(t)$. The solid curve is computed on $\frac{1}{3}$ step of Fig. 1(a). The dashed curve is computed on $\frac{1}{2}$ step of Fig. 1(b).

By examining the configurations of vortices and flux in the array, it is possible to make a rough description of the vortex motion on the subharmonic steps. We define the vorticity function n_v in each cell to be

$$n_v = \frac{1}{2\pi} M\tilde{\phi} + \frac{\Phi}{\Phi_0} , \tag{18}$$

where the mesh matrix M represents performing a directed sum over the gauge-invariant phase differences of the junctions comprising the cell and Φ is the total flux (applied and induced) through the cell. In defining the vorticity we use phase differences $\tilde{\phi}$, which are obtained from ϕ by requiring $\tilde{\phi}$ to lie in the interval $[-\pi, \pi]$ [if we do not use these restricted phase differences in the sum, then by Eq. (11c), $n_v = n$, which provides no information]. Our definition of the vorticity is essentially the same as that of Ref. 27. For vortices, $n_v = 1$, and for antivortices, $n_v = -1$.

In general, in an $N \times N$ array in zero field, we find that the (subharmonic) $\frac{1}{k}$ Shapiro steps result from N vortices and antivortices moving across the array and annihilating in the interior, with this process having a period k times the period of the ac drive. The precise motion of the vortices, however, depends on $\lambda_\perp$ and k. On the integer steps ($k = 1$), for all $\lambda_\perp$, we find that on each ac cycle one column of N vortices and one column of N antivortices move from opposite edges of the array to the center, where they annihilate. A typical instantaneous vortex configuration is shown in Fig. 4(c).

The mechanism for the zero-field $\frac{1}{2}$ steps ($k = 2$), on the other hand, is dependent on $\lambda_\perp$. We can distinguish three separate regimes: $\lambda_\perp > N$, $N > \lambda_\perp > 1$, and $\lambda_\perp < 1$. For approximately $\lambda_\perp > N$, no subharmonic $\frac{1}{2}$ steps are observed. In the small arrays, for $N > \lambda_\perp > 1$, on every other ac cycle columns of m (m is about $N/2$) isolated vortices move across the array and annihilate with antivortices entering from the opposite edge. On the alternate ac cycles, $N - m$ vortices and antivortices cross the array, so that the net effect is to move N vortices (antivortices) across the array in a time of twice the period of the ac drive. Figures 4(a) and 4(b) show typical instantaneous vortex configurations on each part of the cycle. In this particular state [corresponding to $\nu_I = 2.0\nu_c$, $\lambda_\perp = 2.0$, $I_{\rm ac} = 2.0$, as in Fig. 2(b)], seven vortices and antivortices have entered from the edges, and annihilate in the center. Then, four vortex–anti-vortex pairs form *in the center of the array* at the interstices of the pattern formed by the seven vortex–anti-vortex pairs that just annihilated. These sets of four vortices (antivortices) collide with a column of eleven antivortices or vortices that enter from the array edge, to reproduce the original configuration of seven vortices, the entire process having a period twice that of the ac drive.

In contrast, when $\lambda_\perp < 1$, a column of N vortices moves across the array to annihilate with a column of N antivortices moving in from the opposite edge, just as on an integer step [Fig. 4(c)], except that the motion has period $2/\nu_I$. The mechanism for the higher-order steps is similar; i.e., on the $\frac{1}{3}$ step a column of N vortices and one of N antivortices move across the array and annihilate [the instantaneous vortex configuration are again similar to Fig. 4(c)].

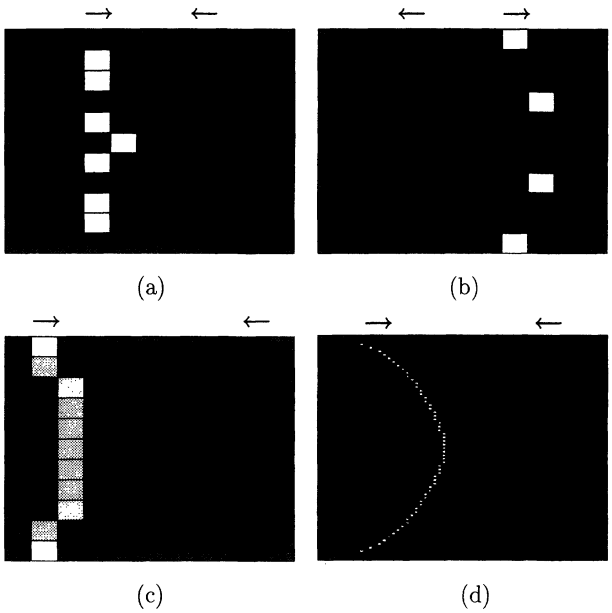

FIG. 4. (a) Typical instantaneous vortex configurations in arrays. The white squares are vortices (moving left to right) and black squares are antivortices (moving right to left). Current flows from top to bottom of array. (a) Vortex configuration on zero-field subharmonic $\frac{1}{2}$ step for $\lambda_\perp > 1$ in small arrays: first part of cycle. (b) Vortex configuration on zero-field subharmonic $\frac{1}{2}$ step for $\lambda_\perp > 1$ in small arrays: second part of cycle. (c) Vortex configuration on zero-field subharmonic steps for $\lambda_\perp < 1$ and integer giant Shapiro steps for all $\lambda_\perp$. (d) Vortex configuration on $\frac{1}{2}$ step in 63×63 array, $\lambda_\perp = 4$, $\beta_c = 0$, $\nu = 2\nu_c$, $I_{\rm ac} = 2I_c$, and $I_{\rm dc} = 1.21I_c$. For this array, vortex configurations on other steps are similar.

In our simulations of larger arrays, this latter sort of vortex motion, where the vortices move in columnlike formations, seems to be predominant at all $\lambda_\perp$. Figure 4(d) shows an instantaneous vortex configuration for a 63×63 array, with $\lambda_\perp = 4$, biased on the $\frac{1}{2}$ subharmonic step. Possibly the ratio $\lambda_\perp/N$, which will affect the force felt by vortices at the edge of the array (see the next section), determines the configuration of the vortices that enter the array.

In Ref. 2 experimental evidence was presented which indicated that the subharmonic steps were associated with the self-fields in the array. It was proposed that the $\frac{1}{2}$ step was due to the nucleation of a commensurate $f = \frac{1}{2}$ vortex state at the edges of the array as a result of the self-field of the array currents. In Ref. 3, however, subharmonic steps were observed in arrays where the induced field strength would be too weak to nucleate an $f = \frac{1}{2}$ or $\frac{1}{3}$ vortex state at the edges of the array. The simulations of Ref. 11, using a truncated inductance model, demonstrated subharmonic $\frac{1}{2}$ steps arising from inductive effects, but apparently no induced commensurate state was observed. Our results with the full inductance model clearly indicate the presence of the subharmonic steps, even at fairly weak self-field strength, but we find no evidence for the formation of any special vortex

states near the edge (in fact, as discussed above, vortices moving in the array do not even always nucleate at the edge). Arrays that exhibit spatial symmetry about the direction of the applied current do not exhibit subharmonic response;[28] it now appears likely that the self-fields are one possible symmetry-breaking mechanism, which allows subharmonic array response.

B. Screening effects

Some other effects of the self-fields on the ac response of a Josephson array can be explained in terms of "screening" effects due to self-fields. Including inductive effects in the description of the Josephson array introduces the characteristic length scale $\lambda_\perp$. $\lambda_\perp$ determines how quickly magnetic excitations decay in the array, and thus establishes the interaction range of vortices and junctions when self-fields are considered. We show that the ability of an array to phase lock to the applied current is limited by how small $\lambda_\perp$ is relative to the size of the array.

As an example of how the I-V characteristics change as the system size increases with $\lambda_\perp$ fixed, consider Fig. 5(a), which shows the I-V characteristics of a 63×63 array with parameters similar to the array of Fig. 1(b) ($\lambda_\perp = 1$, $\nu = 0.6\nu_c$, $I_{\rm ac} = I_c$, zero applied field). Steplike structure is clearly visible at $\frac{1}{2}$ and $\frac{2}{3}$, as in the small arrays. A notable difference between Fig. 5(a) and Fig. 1(b) is the shape of the curve around the integer step. The I-V characteristic of Fig. 5(a) is rounded on the rising side of the step, so that the region over which the array is phase locked on the first integer step is considerably reduced.

For a possible explanation of the step-width reduction, first consider how an applied current redistributes itself under the influence of the self-fields. The self-consistently computed distribution of a small dc current in the array can be obtained by setting the time derivatives of Eq. (11) to zero and solving the resulting nonlinear system of equations using Newton's method.[13] Inspection of current variables in time-dependent simulations indicates that the behavior of larger amplitude and time-varying applied currents is similar. The bold solid curve of Fig. 5(b) shows a cross section of a computed current distribution in a 63×63 array, with $\lambda_\perp = 2$, in the absence of vortices and applied field. The cross section is taken along the direction perpendicular to the applied current. The effect of the self-fields is to cause the current (supercurrent or normal current) to bunch up near the edges of the array. Note that as the current is injected uniformly but is nonuniform in the array center, the current distribution in the array also varies in the direction parallel to the direction of current injection. Effectively, different junctions in the array are driven with differing applied currents, reducing the ability of the whole array to lock to the ac driving current. As the degree of inhomogeneity of the distribution of applied current increases with decreasing $\lambda_\perp/N$, we expect the ability of the array to phase lock to also decrease as $\lambda_\perp/N$ becomes small (although due to the discrete nature of the array, there may be a saturation for $\lambda_\perp < 1$). This indicates that self-field effects are very important in determining the I-V characteristics of large arrays, even where relatively weak ($\lambda_\perp \gg 1$) induced fields are present.

A possible measure of the strength of phase-locking in the array is the range of dc bias currents $\Delta I_{\rm dc}$, at fixed frequency ν_I and ac drive $I_{\rm ac}$, over which the array is on a Shapiro step. Figure 5(c) shows the range of dc bias current $\Delta I_{\rm dc}$ over which square arrays of various sizes N

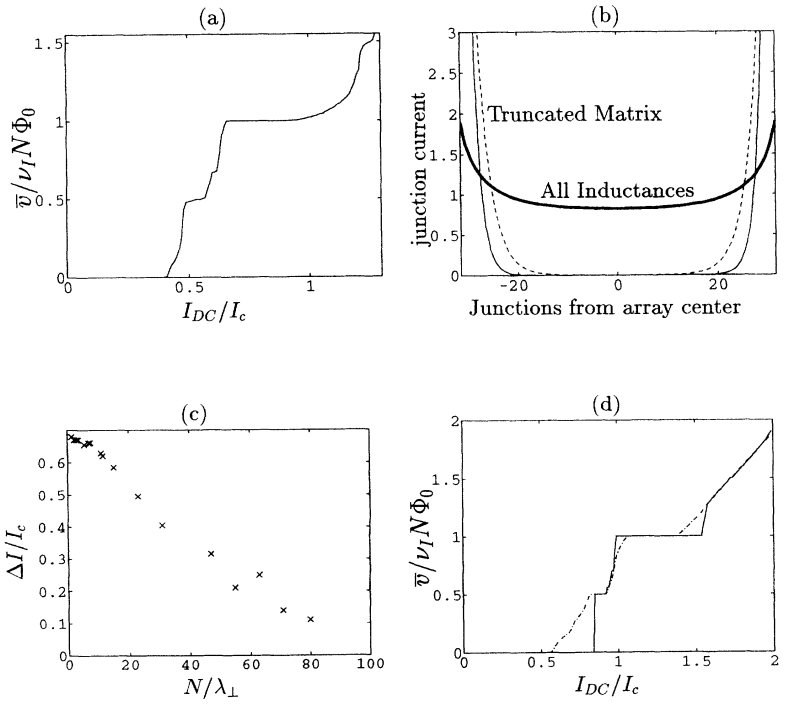

FIG. 5. (a) I-V characteristic of 63×63 Josephson-junction array, $\lambda_\perp = 1$, $\nu_I = 0.6\nu_c$, $I_{\rm ac} = I_c$, $\beta_c = 0$. (b) The distribution of current in a cross section of a 63×63 array, $\lambda_\perp = 2$. Bold curve: all inductances. Light solid curve: only self-inductances included in calculating induced fields. Light dashed curve: self- and near-neighbor-inductances included. All curves normalized to the (uniform) junction current which would flow at $\lambda_\perp = \infty$. (c) The width of integer giant Shapiro step as affected by self fields. $\Delta I/I_c$ is width of first integer giant Shapiro step for $N \times N$ arrays, $\nu_I = 0.6\nu_c$, $I_{\rm ac} = I_c$, and $\beta_c = 0$. N varied from 7 to 80, $\lambda_\perp$ varied from 1.0 to 5.0 for small arrays, $\lambda_\perp = 1.0$ for large ($N > 31$) arrays. (d) Zero-field I-V characteristics of ac-driven 11×11 array, $\beta_c = 0.7$, $\nu_I = 1.0\nu_c$, $f = 0.0, I_{\rm ac} = I_c$, and $\lambda_\perp = 0.1$. Dashed curve is for array in free space, solid curve for array with ideal ground plane located $0.1p$ away.

and penetration depths $\lambda_\perp$ can lock on the first integer step when $\nu_I = 0.6\nu_c, I_{ac} = I_c$. We define ΔI_{dc} to be the range of dc currents over which the array voltage is at the Shapiro step voltage and precisely periodic. This corresponds to the precisely flat region of the I-V characteristic [about $0.7I_c$ to $0.9I_c$ in Fig. 5(a)]. The range of phase-locking $\Delta I/I_c$ decreases with increasing $N/\lambda_\perp$, as would be predicted by the preceding argument. Our calculations appear to be in general agreement with the experiments of Refs. 1 and 8.

These general observations are in accord with the experimental observations of Ref. 14, where it was indicated that inductive effects should not be too large in order to observe coherent array oscillations. The dashed curve of Fig. 5(d) shows a computed I-V curve for an array with parameters similar to Refs. 12 and 14. In contrast to the calculations of Figs. 1 and 2, which were intended to model heavily overdamped superconductor–normal-metal–superconductor (SNS) -type arrays, the superconductor-insulator-superconductor (SIS) arrays of Refs. 12 and 14 generally have non-negligible junction capacitance, which we have taken into account when calculating Fig. 5(d).

An obvious way to minimize self-field effects is to place a ground plane under the array, as may also be present in fabricated SIS junction circuits (e.g., Refs. 12 and 14). An ideal ground plane is easily treated in the formalism of Sec. II by using image currents to modify the construction of the inductance matrix. When the ideal ground plane is placed $0.1p$ away from the array, as shown in the solid curve of Fig. 5(d), some of the deleterious effects of the self-fields are eliminated. Compared to the array without a ground plane, shown by the dashed curve, the first integer step is wider and sharper, indicating a greater tendency for the junctions in the array to all phase-lock to the applied current. For these parameters (11×11 array, $\beta_c = 0.7, \lambda_\perp = 0.1, \nu_I = \nu_c, I_{ac} = I_c$), however, the subharmonic $\frac{1}{2}$ step remains in the presence of the ground plane (presumably due to the finite capacitance of the junctions), although it becomes smaller.

C. Approximate inductance models

An issue related to the screening effects discussed in the preceding section is the effect on the calculated array response when an approximate model is used for the inductance matrix, as the simulated magnetic response of the array changes when the inductance matrix is truncated. In order to reduce the computational complexity of including induced magnetic fields in simulations of Josephson junction arrays, it is common[15,16,11] to consider a truncated[29] inductance matrix. The full mutual inductance matrix is a complete representation of an integral formulation of Maxwell's equations for the 2D array in free space,[13] but a truncated matrix does not represent the full set of electromagnetic interactions. In this section we shall demonstrate that, particularly under current bias, models for the array using the truncated inductance matrix can result in computed currents and fields which are physically unrealistic.

We discuss two truncated models for the form of the fields induced in the array. The first model is the self-inductance approximation, where the induced field in a cell is due only to the mesh current circulating in the same cell (i.e., the matrix $L = ML^bM^T$ is diagonal, with diagonal entry the self-inductance L_s). The self-inductance approximation corresponds to the case where the fields have components only in the direction perpendicular to the plane containing the array.[15,16] The second model includes near-neighbor corrections to the self-inductance, where the induced field in a cell depends on the mesh current flowing in it and the four nearest-neighboring cells. In addition to specifying the form of L, the form of the fields directly induced by the applied currents (which in the full inductance case would be ML^bI_s) must be specified.

There are two approaches to modeling the fields induced by the applied currents. We may truncate the matrix ML^b, retaining terms that would contribute to the self- or near-neighbor-inductance coefficients. A more consistent approach to modeling the fields induced in the array is to consider the array as extended by one cell, with the applied currents flowing in the fictitious border cell. Thus in the self-inductance case the induced fields depend only on the mesh current flowing in the array, $\Phi^{ind} = L_sI_m$, with no contribution from the applied currents I_s (although of course in the self-consistent calculation I_m is implicitly dependent on I_s). When near-neighbor mutual inductances are included, the fields induced by I_s are non-zero only in a cell at the edge of the array and are given by the product of the near-neighbor-inductance coefficient and the current in the fictitious cell. Thus at the edges of the array, in the near-neighbor-inductance case these fields are proportional to $\pm I_e$, where I_e is the externally applied current.

Figure 5(b) shows the effect of the inductance model on the distribution of an applied current in the Josephson array (63×63 array, with $\lambda_\perp = 2$). The solid bold curve shows a cross section of the computed current distribution when all inductances are included in the model. After a fairly rapid decrease near the edge, the current density becomes essentially constant in the center of the array. In contrast, when the inductance matrix is truncated, as shown by the light curves of Fig. 5(b), the current distribution falls off very rapidly near the edge of the array and becomes essentially zero inside. When modeling the self-fields by using only a single self-inductance term (light solid curve), the characteristic length changes to $\lambda_J \simeq \lambda_\perp^{1/2}$, and excitations decay exponentially rather than algebraically. As discussed in Ref. 13, including small numbers of off-diagonal terms in the inductance matrix alters the penetration depth, but does not change the functional form of the current distribution, as can also be seen from the light dashed curve of Fig. 5(b). For example, it can be shown that the penetration depth changes from λ_J^2 in the self-inductance case to $\lambda_J'^2 = \lambda_J^2/(1-4M/L)$ when near-neighbor-inductances are included, where L and M are the self- and near-neighbor-inductance coefficients, respectively. The current distributions are qualitatively different in that for a fixed $\lambda_\perp$, as $N \to \infty$, when the truncated matrix is con-

sidered, the region of the array more than a few $\lambda_\perp$ from the edges will carry essentially zero net current, whereas when the full matrix is considered there will *always* be a finite net current in this region.[30] For example, even in a 511 × 511 cell array, with $\lambda_\perp = 0.1$, the calculated current in the center of the array is 75% of its value when $\lambda_\perp = \infty$. Thus, the treatment of induced fields by using the approximate, truncated inductance matrices results in simulation of arrays with unrealistically strong screening properties.

The effect on the array's *I-V* characteristics of truncating the mutual inductance matrix is shown by the curve of Fig. 6. The *I-V* curve of Fig. 6 was computed using the same parameters as the curve of Fig. 1(b) but with a truncated inductance matrix (only a self inductance was included in this model). The *I-V* characteristic has a considerably different form: the critical current is suppressed, the width of the integer giant step is reduced and the curve is generally more "smeared out." Because of the exponential form of the current screening, when $\lambda_J \ll N$, there is very little current in the array center as compared to the edges, so the range of dc current biases over which the entire array can phase lock to the applied current is reduced. In contrast, when the full inductance matrix is considered, there is always some current in the interior of the array, so the Shapiro step structure persists to much higher $\lambda_\perp/N$. Note that subharmonic structure, as indicated by the $\frac{3}{2}$ step, is still evident in this curve, even though only a self-inductance was used to calculated the induced fields.[34] We have observed similar differences between the *I-V* characteristics of arrays where the full inductance matrix was used in the simulation and arrays where self- and near-neighbor inductances were included, indicating that including near-neighbor inductances does not substantially improve the self-inductance approximation.

The effect of the choice of inductance model can also be seen in the configuration and motion of vortices in the array. When only a few inductances are included in the calculation the driving current is more severely bunched up near the edge, and so vortices are easily pulled into the array, but once they are a few penetration depths $\lambda_J \simeq \lambda_\perp^{1/2}$ from the edge the vortices are nearly unaffected by the driving current. When the array is wider than a few λ_J, the force acting on vortices is strong near the edge but very weak in the center. Vortices may be quickly pulled into the array, but then sluggishly move across and bunch up in the interior before annihilating. At this point, there is essentially no interaction between widely separated junctions. In contrast, when the full inductance matrix is used in the calculation, the applied current can accelerate the vortices across the entire width of the array, so that single columns of vortices and antivortices quickly cross the array and annihilate in the center, as in Fig. 4(d). When the full inductance matrix is used in the calculation, occasionally two columns of vortices and antivortices are observed to exist simultaneously in very large arrays, but never do we observe the high vortex–anti-vortex densities present when using the approximate inductance models.

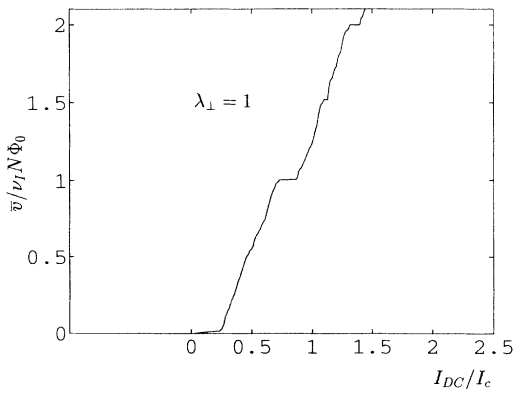

FIG. 6. Zero-field *I-V* characteristics of ac-driven 11 × 11 cell array, $\beta_c = 0.0$, $\nu_I = 0.6\nu_c$, $f = 0.0$, $I_{ac} = I_c, \lambda_\perp = 1$, with only a self-inductance included in calculating the induced fields. Axes have been chosen to provide the same scales as Fig. 1(b). Note the subharmonic step at $\frac{3}{2}$.

IV. CONCLUSION

We have shown that self-field effects are important in determining the behavior of Josephson-junction arrays driven with ac currents, even when the self-fields are fairly weak (for example, arrays with $\lambda_\perp = 10$ can still exhibit subharmonic Shapiro steps under some bias conditions). In zero magnetic field, self-field effects can produce subharmonic Shapiro steps in Josephson arrays: $\frac{1}{2}$ steps are the strongest, but higher-order steps, such as at $\frac{1}{3}$ have also been observed. Our results suggest that any detailed understanding of the subharmonic response of Josephson-junction arrays must consider self-field effects. A more detailed study of such characteristics as, for example, the frequency and bias-current dependence of the subharmonic step widths, is desirable.

Strong self-fields can reduce the strength of phase locking to an external oscillating current drive, as evidenced by a reduction in the range of biases over which the array is on an integer giant Shapiro step. We expect many of the conclusions of this paper to apply to the case of mutual phase locking in the array as well. It is well known,[31] for example, that 1D arrays with short interaction lengths exhibit weak phase-locking properties. Thus, in practical applications of 2D Josephson arrays, it would be desirable to minimize self-field effects. However, an accurate description of the array dynamics must include mutual inductance interactions between all cell pairs in the array.

ACKNOWLEDGMENTS

We gratefully acknowledge support from NSF Grant No. DMR-9108748 and an IBM equipment grant. J.W. acknowledges support from NSF Grant No. MIP-8858764 A02, and from Defense Advanced Research Projects Agency Contract No. N00014-91-J-1698. J.R.P. acknowledges support from DOD.

APPENDIX: TREATMENT OF STIFF SYSTEMS

When the system of differential equations describing the Josephson array is stiff, simulations can be performed more efficiently and robustly if time discretization is performed using stiffly-stable backward difference formulas.[22,32,33] Such methods can be directly applied to the differential-algebraic system of Eq. (11). In general, time discretization of an ODE of the form $dx/dt = f(x,y,t)$ by the backward difference formulas given a constraint $g(x,y) = 0$ leads to nonlinear systems of the form

$$\hat{x} - \alpha f(\hat{x},\hat{y}) - r = 0 \ , \tag{A1a}$$

$$g(\hat{x},\hat{y}) = 0 \ , \tag{A1b}$$

where x, y are the solution vectors, $\hat{x}, \hat{y}$ are numerical approximations to x, y at a specific timepoint, α is a constant, and r is some constant vector, which may depend on approximations to x at previous timepoints. Newton's method[23] applied to solving a nonlinear system of this form consists of the repeated iteration

$$J(\hat{x}^k,\hat{y}^k)\begin{bmatrix}\delta\hat{x}^k\\ \delta\hat{y}^k\end{bmatrix} = \begin{bmatrix}-\hat{x}^k + \alpha f(\hat{x}^k,\hat{y}^k) + r\\ -g(\hat{x}^k,\hat{y}^k)\end{bmatrix} \tag{A2}$$

with

$$\hat{x}^{k+1} = \hat{x}^k + \delta\hat{x}^k \ ,$$
$$\hat{y}^{k+1} = \hat{y}^k + \delta\hat{y}^k \ ,$$

where J is the Jacobian matrix,

$$J(\hat{x}^k,\hat{y}^k) = \begin{bmatrix} I - \alpha\frac{\partial f}{\partial x}\Big|_{\hat{x}^k,\hat{y}^k} & -\alpha\frac{\partial f}{\partial y}\Big|_{\hat{x}^k,\hat{y}^k} \\ \frac{\partial g}{\partial x}\Big|_{\hat{x}^k,\hat{y}^k} & \frac{\partial g}{\partial y}\Big|_{\hat{x}^k,\hat{y}^k}\end{bmatrix} \ , \tag{A3}$$

I is the identity matrix, and the superscript k indicates evaluation of a quantity at Newton iteration k. The iteration is terminated when Eq. (A1) is satisfied to within some specified tolerance. Applying the general forms of Eqs. (A1)–(A3) to the DAE system of Eq. (11) leads to the iteration

$$\begin{bmatrix} I & -\gamma\beta_c I & 0 \\ \gamma C & I(1+\gamma) & -\gamma M^T \\ M & 0 & \frac{1}{\lambda_\perp}\Lambda\end{bmatrix}\begin{bmatrix}\delta\phi^k\\ \delta v^k\\ \delta I_m^k\end{bmatrix} = -\begin{bmatrix}f_1^k\\ f_2^k\\ f_3^k\end{bmatrix} \tag{A4a}$$

$$\phi^{k+1} = \phi^k + \delta\phi^k \quad v^{k+1} = v^k + \delta v^k \quad I_m^{k+1} = I_m^k + \delta I_m^k, \tag{A4b}$$

where the matrix C in the Jacobian is diagonal with entries given by

$$C_{ii} = \cos\phi_i^k, \tag{A5}$$

$\gamma \equiv 2\pi\alpha/\beta_c$, and

$$\begin{bmatrix}f_1^k\\ f_2^k\\ f_3^k\end{bmatrix} = \begin{bmatrix} -\phi^k + 2\pi\alpha v^k + r_1 \\ -v^k + \gamma(M^T I_m^k - \sin\phi^k - v^k + I_s) + r_2 \\ -[M\phi^k + \frac{1}{\lambda_\perp}(\Lambda I_m + M\Lambda^b I_s) - 2\pi(n-f)]\end{bmatrix}. \tag{A6}$$

Eliminating the variables $\delta\phi^k$ and δv^k from Eq. (A4) by performing block Gaussian elimination results in the reduced system

$$\left[\frac{1}{\lambda_\perp}\Lambda + MDM^T\right][\delta I_m^k] = \left[f_3 - MD\left(f_2 + \frac{1+\gamma}{\gamma\beta_c}f_1\right)\right], \tag{A7}$$

where the matrix D is diagonal with entries

$$D_{ii} = \frac{\gamma^2\beta_c}{\gamma^2\beta_c\cos\phi_i + \gamma + 1}. \tag{A8}$$

The application of the iterative algorithm (GMRES) to solve Eq. (A7) then proceeds as described in Ref. 13. To construct a preconditioner in which accelerates GMRES convergence, we simplify Eq. (A8) by assuming $\phi = 0$. An effective preconditioner $P^{-1} \simeq [\frac{1}{\lambda_\perp}\Lambda + MDM^T]$ is then given by

$$P^{-1} = \frac{1}{\lambda_\perp}\tilde{\Lambda} + \frac{\gamma^2}{\gamma^2\beta_c + \gamma + 1}MM^T. \tag{A9}$$

P can be computed in $O(N\log_2 N)$ time by use of fast sine transforms.

[1] S. P. Benz, M. S. Rzchowski, M. Tinkham, and C. J. Lobb, Phys. Rev. Lett. **64**, 693 (1990).
[2] H. C. Lee, R. S. Newrock, D. B. Mast, S. E. Hebboul, J. C. Garland, and C. J. Lobb, Phys. Rev. B **44**, 921 (1991).
[3] S. E. Hebboul and J. C. Garland, Phys. Rev. B **43**, 13 703 (1991).
[4] K. H. Lee, D. Stroud, and J. S. Chung, Phys. Rev. Lett. **64**, 962 (1990).
[5] J. U. Free, S. P. Benz, M. S. Rzchowski, M. Tinkham, C. J. Lobb, and M. Octavio, Phys. Rev. B **41**, 7267 (1990).
[6] K. H. Lee and D. Stroud, Phys. Rev. B **43**, 5280 (1991).
[7] M. Octavio, J. U. Free, S. P. Benz, R. S. Newrock, D. B. Mast, and C. J. Lobb, Phys. Rev. B **44**, 4601 (1991).
[8] S. E. Hebboul and J. C. Garland, Phys. Rev. B **47**, 5190 (1993).
[9] D. Domínguez, J. V. José, and A. Karma, Phys. Rev. Lett. **67**, 2367 (1991).
[10] W. Yu, E. B. Harris, S. E. Hebboul, J. C. Garland, and D. Stroud, Phys. Rev. B **45**, 12 624 (1992).
[11] D. Domínguez and J. V. José, Phys. Rev. Lett. **69**, 514 (1992).
[12] S. P. Benz and C. J. Burroughs, Appl. Phys. Lett. **58**, 2162 (1991).
[13] J. R. Phillips, H. S. J. van der Zant, J. White, and T. P. Orlando, Phys. Rev. B **47**, 5219 (1993).
[14] S. P. Benz and C. J. Burroughs, Supercond. Sci. Technol. **4**, 561 (1991).
[15] K. Nakajima and Y. Sawada, J. Appl. Phys. **52**, 5732

(1981).
[16]A. Majhofer, T. Wolf, and W. Dieterich, Phys. Rev. B **44**, 9634 (1991).
[17]C. A. Desoer and E. S. Kuh, *Basic Circuit Theory* (McGraw-Hill, New York, 1969).
[18]T. P. Orlando, J. E. Mooij, and H. S. J. van der Zant, Phys. Rev. B **43**, 10 218 (1991).
[19]E. Hairer, S. P. Norsett, and G. Wanner, *Solving Ordinary Differential Equations I, Nonstiff Problems* (Springer-Verlag, Berlin, 1987).
[20]G. H. Golub and C. F. V. Loan, *Matrix Computations* (Johns Hopkins University Press, Baltimore, 1989).
[21]Y. Saad and M. Schultz, SIAM J. Sci. Stat. Comput. **7**, 856 (1986).
[22]E. Hairer and G. Wanner, *Solving Ordinary Differential Equations II, Stiff and Differential-Algebraic Problems* (Springer-Verlag, Berlin 1991).
[23]J. Stoer and R. Bulirsch, *Introduction to Numerical Analysis* (Springer-Verlag, New York, 1980).
[24]G. D. Byrne and A. C. Hindmarsh, ACM Trans. Math. Software **1**, 71 (1975).
[25]P. Brown, G. D. Byrne, and A. C. Hindmarsh, SIAM J. Sci. Statist. Comput. **10**, 1038 (1989).
[26]A. V. Oppenheim and R. W. Schafer, *Discrete-Time Signal Processing* (Prentice-Hall, Englewood Cliffs, 1989).
[27]U. Geigenmuller, C. J. Lobb, and C. B. Whan, Phys. Rev. B **47**, 348 (1993).
[28]L. L. Sohn, M. S. Rzchowski, J. U. Free, and M. Tinkham, Phys. Rev. B **45**, 3003 (1992).
[29]In the notation of Ref. 13, induced fields are often approximated by truncating the mesh inductance matrix L. Another option is to truncate the *branch* inductance matrix, L_b. Although neither approach results in equations, which correspond to a physical system, truncating L_b is more likely to create computational difficulties. This is because for 2D arrays the L matrix is an M matrix [see R. S. Varga, *Matrix Iterative Analysis* (Prentice-Hall, Englewood Cliffs, New Jersey, 1962)], and therefore will remain positive-definite regardless of how many off-diagonal terms are discarded. However, truncating L_b often results in an indefinite matrix, which if used in a numerical calculation can result in unstable computed solutions.
[30]E. H. Rhoderick and E. M. Wilson, Nature (London) **194**, 1167 (1962).
[31]A. K. Jain, K. K. Likharev, J. E. Lukens, and J. E. Sauvageau, Phys. Rep. **109**, 309 (1984).
[32]C. W. Gear, IEEE Trans. Circuit Theory **18**, 89 (1971).
[33]K. E. Brenan, S. L. Campbell, and L. R. Petzold, *Numerical Solution of Initial-Value Problems in Differential-Algebraic Equations* (Elsevier, Amsterdam, 1989).
[34]We should note that no subharmonic steps were observed in Ref. 11 when only self inductances were used in the calculation. However, subharmonic steps should be observed even when only a self inductance is included in the calculation of the induced fields, since the induced fields, when computed self-consistently, will always be antisymmetric regardless of the inductance model considered. More precisely, in the presence of a self inductance L_s, the induced fields are $\Phi^{\text{ind}} = L_s I_m$ and in the limit of small I_s, $I_m = -(MM^T + L_s I)^{-1} M I_s$, which will always be antisymmetric about a plane through the center of the array parallel to the direction of applied current.